



Why observed and modelled ozone production rates and sensitivities differ, a case study at rural site in CHINA

Bowen Zhong^{1#}, Bin Jiang^{1#}, Jun Zhou^{1*}, Tao Zhang², Duohong Chen², Yuhong Zhai², Junqing Luo¹, Minhui Deng¹, Mao Xiao^{3,4}, Jianhui Jiang^{5,6}, Jing Li¹, Min Shao^{1*}

5 ¹College of Environment and Climate, Institute for Environment and Climate Research, Guangdong-Hongkong-Macau Joint Laboratory of Collaborative Innovation for Environmental Quality, Jinan University, Guangzhou 511443, China

²Environmental Key Laboratory of Regional Air Quality Monitoring, Ministry of Ecology and Environment, Guangdong Ecological and Environmental Monitoring Center, Guangzhou 511443, China

³Sichuan Academy of Environmental Sciences, Chengdu 610041, China

10 ⁴Biogas Institute of Ministry of Agriculture and Rural Affairs, Chengdu 610041, China

⁵Global Institute for Urban and Regional Sustainability, School of Ecological and Environmental Sciences, East China Normal University, Shanghai 200241, China

⁶Institute of Eco-Chongming, East China Normal University, Shanghai 200241, China

15 [#]These authors contribute equally to this article

*Correspondence to: Jun Zhou (junzhou@jnu.edu.cn) & Min Shao (mshao@jnu.edu.cn)

Abstract. Ground-level ozone (O_3) pollution has recently become of increasing concern in China. Studies have shown that conventional models often fail to predict accurately the net O_3 production rate ($P(O_3)_{net}$) due to the absence of certain mechanisms, particularly the kinetics from missing reactive volatile organic compounds (VOCs) species, and hence affects the reliability of evaluation for O_3 formation sensitivity (OFS). Therefore, we conducted a field observation of $P(O_3)_{net}$ and OFS using a $P(O_3)_{net}$ (NPOPR) detection system based on a dual-channel reaction chamber technique at the Guangdong Atmospheric Supersite of China in Heshan, Pearl River Delta (PRD) in autumn of 2023. The in-situ monitoring data were then compared with results from a zero-dimensional model incorporating the Master Chemical Mechanism (MCM v3.3.1). We tested the model performance by incorporating parameterization for 4 processes including HO_2 uptake by ambient aerosols, dry deposition, N_2O_5 uptake, and $ClNO_2$ photolysis, and found that the discrepancies between the modelled $P(O_3)_{net}$ ($P(O_3)_{net_Mod}$) and measured data ($P(O_3)_{net_Mea}$) did not change evidently, the maximum daily $P(O_3)_{net}$ differed by ~44.8 %. Meanwhile, we found that the agreement of OFS assessment results between the direct measurements and the modelling study was lower in the $P(O_3)_{net}$ rising phase (08:00-09:00, 63.6%) than in the $P(O_3)_{net}$ stable phase (10:00-12:00, 72.7%) and $P(O_3)_{net}$ declining phase (13:00-17:00, 72.7 %). The only approach to fill the gap between observation and computation was to add possible unmeasured reactive VOCs, especially oxygenated VOCs (OVOCs) in box model, this was true for both $P(O_3)_{net}$ and consequent OFS, hinting clearly at the importance of quantitative understanding the total reactivity of VOCs in O_3 chemistry.

1 Introduction

Ground-level ozone (O_3) pollution has garnered widespread attention due to its adverse effects on human health (Chen et al., 2023), vegetation growth (Wang et al., 2017), and climate change (Li et al., 2016). Since the implementation of the *Air Pollution Prevention and Control Action Plan* by the State Council in 2013, particulate matter pollution in China has significantly decreased. However, ground-level O_3 pollution remains severe, and O_3 has become the primary pollutant affecting



air quality in China (*China Environmental Status Bulletin*, 2013–2024). The variation in ground-level O₃ concentration is influenced by local photochemical production, surface deposition, and transport processes, which the following equation can express:

40
$$\frac{\partial [O_3]}{\partial t} = P(O_3)_{\text{net}} - \frac{u_d}{H} [O_3] - \nu \cdot \nabla [O_3] \quad (1)$$

In Equation (1), $\frac{\partial [O_3]}{\partial t}$ represents the change in O₃ concentration, $P(O_3)_{\text{net}}$ denotes the net O₃ photochemical production

rate, u_d is the O₃ deposition rate, H stands for the mixed layer height, and ν represents the wind speed. The in-situ photochemical production of ground-level O₃ primarily results from the photochemical reactions of precursor volatile organic compounds (VOCs) and nitrogen oxides (NO_x: NO+NO₂) under sunlight. The $P(O_3)_{\text{net}}$ is a critical indicator for evaluating 45 local photochemical formation. The budget analysis of ground-level O₃ production ($P(O_3)$) and consumption ($D(O_3)$) can be calculated using the following equation:

$$P(O_3) = k_{HO_2+NO} [HO_2] [NO] + \sum_i k_{RO_{2i}+NO} [RO_{2i}] [NO] \varphi_i \quad (2)$$

$$D(O_3) = k_{O(^1D)+H_2O} [O(^1D)] [H_2O] + k_{OH+O_3} [OH] [O_3] + k_{HO_2+O_3} [HO_2] [O_3] \\ + \sum_i (k_{O_3+Alkene_i} [O_3] [Alkene_i]) + k_{OH+NO_2} [OH] [NO_2] + k_{RO_{2i}+NO_2} [RO_{2i}] [NO_2] \quad (3)$$

$$P(O_3)_{\text{net}} = P(O_3) - D(O_3) \quad (4)$$

50 Equations (2)–(4) illustrate the nonlinear dependence of the $P(O_3)_{\text{net}}$ on the oxidation of precursors generating HO_x (=OH+HO₂) (Tong et al., 2025). Here, the $P(O_3)_{\text{net}}$ is the difference between $P(O_3)$ and $D(O_3)$, k_{M+N} is the reaction rate constant between two molecules, φ_i represents the amount of NO₂ generated from the reaction of RO_{2i} with NO₂, and i denotes different RO₂ species. Currently, mainstream model simulation methods for calculating the $P(O_3)_{\text{net}}$ primarily involve indirectly solving 55 radical concentrations. However, existing models cannot fully characterize the complex radical cycling processes in the real atmosphere (Wei et al., 2023). Specifically, the incomplete mechanisms of RO_x (=OH+HO₂+RO₂) sources are particularly prominent, and these missing mechanisms affect the accuracy of RO₂ and HO₂ radical estimations to varying degrees. These include the neglect of contributions from carbonyl compounds, HONO, and OVOCs (Xu et al., 2022), as well as incomplete mechanisms for heterogeneous reactions on aerosol surfaces (Yang et al., 2022), dry deposition (Zhang et al., 2003), nitrosyl chloride photolysis (Whalley et al., 2021), and isomerization of isoprene peroxy radicals (Kanaya et al., 2012) remain 60 inadequately understood. These gaps lead to systematic biases in the simulated $P(O_3)_{\text{net}}$ (Woodward-Massey et al., 2023; Tan et al., 2017; Tan et al., 2019), thereby affecting the accurate determination of O₃ formation sensitivity (OFS).

It is noteworthy that there is a strong causal relationship between the aforementioned mechanistic biases and the misjudgment of OFS. Studies by Baier et al. (2017) and Tan et al. (2019) found that the observation-based model (OBM) significantly underestimates $P(O_3)_{\text{net}}$ under high NO_x conditions, leading to misjudgment of OFS. They pointed out that the 65 unresolved VOC species and unspecified chemical mechanisms in the model are the primary causes of these biases. Similarly,



70

Whalley et al. (2021) demonstrated that the zero-dimensional (box) model exhibits deviations in simulating $P(O_3)_{net}$ under high VOCs concentrations. Further research by Wang et al. (2024b) highlighted that the contribution of unidentified VOCs reactivity in anthropogenic emissions to O_3 formation is severely underestimated, and the missing VOC species and chemical mechanisms in existing models lead to biases in the determination of OFS. Such diagnostic biases in OFS may result in misjudgment of precursor emission reduction measures, thereby affecting the effectiveness of O_3 pollution control.

75

80

Direct measurement of $P(O_3)_{net}$ based on the dual-reaction chamber technique can address the aforementioned challenges. This concept was first proposed by Jeffries (1971), who suggested determining the real value of the $P(O_3)_{net}$ in ambient air by comparing the difference in $O_X (=O_3+NO_2)$ between a photochemical reaction chamber and a reference chamber. To date, several $P(O_3)_{net}$ detection systems based on the dual-reaction chamber technique have been developed, referred to as measurement of O_3 production sensor (MOPS), O_3 production rate measurement system (O3PR), O_3 production rates instrument (OPRs), net photochemical O_3 production rate detection system (NPOPR), Mea-OPR, or O_3 production rate-cavity ring-down spectroscopy system (OPR-CRDS) (Baier et al., 2015; Sadanaga et al., 2017; Sklaveniti et al., 2018; Hao et al., 2023; Wang et al., 2024c; Tong et al., 2025). Through practical applications in field observations, scholars generally agree that these detection systems offer rapid stability and high precision, with measurement uncertainties around 10 %. Comparative studies have revealed that the underestimation of the simulated $P(O_3)_{net}$ can reach up to 50 % (Cazorla et al., 2012), highlighting the limitations of existing models in characterizing radical chemistry.

85

90

95

More importantly, the $P(O_3)_{net}$ detection system can diagnose OFS by quantifying changes in the measured $P(O_3)_{net}$ induced by different precursors through precursor addition experiments. Sklaveniti et al. (2018) first detected OFS in Indiana by adding NO to the sampling line of $P(O_3)_{net}$ detection systems, demonstrating the feasibility of directly measuring OFS with this device. Morino et al. (2023) combined a smog chamber with the $P(O_3)_{net}$ detection systems to directly measure OFS under baseline environmental conditions in Tokyo during summer. Chen et al. (2024) proposed the OPR_Adj parameter based on the $P(O_3)_{net}$ detection systems, which, through normalization of photolysis rates, diagnosed that O_3 photochemistry in Beijing is under VOCs control. These advancements indicate that the direct measurement method of OFS based on the $P(O_3)_{net}$ not only measures the actual OFS in ambient air but also quantifies the discrepancies between models and measurements.

In this study, we employed the developed NPOPR detection system based on the dual-reaction chamber technique to measure the $P(O_3)_{net}$ and OFS at the Guangdong Atmospheric Supersite of China in Heshan City, Pearl River Delta (PRD), in October 2023. Based on the observational data, we used the box model equipped with the Master Chemical Mechanism (MCM v3.3.1) to simulate the radical chemistry during the observation period. We compared and investigated the differences and influencing factors between the model-simulated values (abbreviated as $P(O_3)_{net}$ Mod) and the directly measured values (abbreviated as $P(O_3)_{net}$ Mea) in calculating the $P(O_3)_{net}$ and assessing OFS.

2 Methods and materials

2.1 Field measurements

Field observations were continuously conducted from 4–26 October 2023 at the Guangdong Atmospheric Supersite of



China in Heshan City, located in northern Jiangmen, Guangdong Province (112.93°E, 22.73°N). The supersite is situated in the downwind area of Guangzhou and Foshan and is characterized by active secondary reactions. It lies at the intersection of forest-agricultural and urban systems, representing a typical rural station. The surrounding area primarily consists of farmland conservation zones and forested areas, with no significant industrial emissions. It is suitable for comprehensive monitoring and research on regional atmospheric complex pollution in the PRD (Mazaheri et al., 2019). The geographical location is shown in Fig. S1.

The $P(O_3)_{\text{net}}$ detection system (NPOPR), based on the dual-reaction chamber technique, was used to monitor the $P(O_3)_{\text{net}}$ and OFS. This system has been successfully applied in multiple field observation campaigns (Hao et al., 2023; Zhou et al., 2024a; 2024b). The detection system consists of a sampling unit, a monitoring unit, and a data acquisition unit. Ambient air passes through a Teflon particulate filter (7592-104, Whatman, UK) to remove particles larger than 2 μm before entering the dual chambers. The reaction chamber and the reference chamber are made of two identical quartz tubes (inner diameter: 190.5 mm, length: 700 mm, wall thickness: 5 mm). Unlike the reaction chamber, which allows ultraviolet light to penetrate and initiate photochemical reactions, the reference chamber is covered with an ultraviolet protective film (SH2CLAR, 3M, Japan) to block light with wavelengths below 390 nm, thereby preventing O_3 formation in the reference chamber. A custom circuit control system alternates the gas flow between the reaction chamber and the reference chamber into the NO reaction tube every 2 minutes, where the O_3 is converted to NO_2 , which is then introduced into a Cavity Attenuated Phase Shift (CAPS)- NO_2 analyzer (Aerodyne Research, Inc., Billerica MA, USA). The gas not introduced into the NO reaction tube is expelled through an auxiliary pump. The data acquisition system detects NO_2 , including both ambient NO_2 and NO_2 converted from O_3 . By combining the average residence time (τ) of the gas in the chambers and the difference in O_x ($\Delta O_x = \Delta(O_3 + NO_2)$) between the two chambers, the $P(O_3)_{\text{net}}\text{-Mea}$ can be calculated. The mean residence time in the reaction chamber is 0.15 h at the air flow rate of 2.1 L min⁻¹. Detailed characterization parameters of the detection system can be found in Hao et al. (2023).

$$P(O_3)_{\text{net}}\text{-Mea} = P(O_x) = \frac{\Delta O_x}{\tau} = \frac{[O_x]_{\text{reaction}} - [O_x]_{\text{reference}}}{\tau} \quad (5)$$

An additional system for the addition of NO or VOCs was added to the NPOPR sampling unit to assess OFS. The OFS was assessed by measuring the changes in $P(O_3)_{\text{net}}$ induced by the addition of NO or VOCs, enabling the direct measurement of OFS. A schematic diagram of this principle is shown in Fig. S2. In the experiments for determining OFS through direct measurements (conducted daily from 8:00-18:00), each cycle lasted 1 hour. The first 20 minutes involved the addition of NO (denoted as $P(O_3)_{\text{net}}\text{-Mea}^{+NO}$), the next 20 minutes measured the ambient baseline ($P(O_3)_{\text{net}}\text{-Mea}$), and the final 20 minutes involved the addition of VOCs (denoted as $P(O_3)_{\text{net}}\text{-Mea}^{+VOCs}$). The concentration of NO added was 20 % of the ambient NO_x concentration at the site, while the concentration of VOCs indicators added was 20 % of the ambient VOCs reactivity. During the observation period, from 4–11 October, the VOCs indicators included isopentane as the representative alkane, ethylene and isoprene as the representative alkenes, and toluene as the representative aromatic hydrocarbon. From 13–26 October, ethylene was used as the representative non-methane hydrocarbon (NMHC) and formaldehyde as the representative oxygenated volatile organic compound (OVOC). The average concentrations of added NO and VOCs during the experiments were 2.8 ppbv and



7.0 ppbv, respectively. The sensitivity of O_3 production to precursor changes was quantified using the measured OFS, derived from the incremental reactivity (IR) index. IR is defined as the change in $P(O_3)_{\text{net}}$ per unit change in precursor concentration ($\Delta S(X)$): a negative IR value indicates that reducing the precursor concentration increases O_3 production (e.g., NO titration effect), while a larger absolute IR value suggests higher sensitivity of O_3 production to changes in the precursor. The IR was calculated as:

$$IR = \frac{P(O_3)_{\text{net}} \text{ Mea}^{+X} - P(O_3)_{\text{net}} \text{ Mea}}{\Delta S(X)} = \frac{\Delta P(O_3)_{\text{net}} \text{ Mea}^{+X}}{\Delta S(X)} \quad (6)$$

where X represents VOCs or NO, $\Delta P(O_3)_{\text{net}}^{+X}$ represents the $P(O_3)_{\text{net}}$ values measured during the NO or VOCs addition period minus the $P(O_3)_{\text{net}}$ values measured when only injecting ambient air. $\Delta S(X)$ represents the concentration of the NO or VOCs precursor added during the corresponding measurement period.

In addition to $P(O_3)_{\text{net}}$ and OFS, hourly data such as $PM_{2.5}$, O_3 , NO, NO_2 , SO_2 , carbon monoxide (CO), photolysis rates (j_{O^1D} , j_{NO_2} , $j_{H_2O_2}$, $j_{NO_3_M}$, $j_{NO_3_R}$, j_{HONO} , j_{HCHO_M} , j_{HCHO_R}), HONO, and VOCs concentrations were monitored (more details about the measurements are shown in Table S1). Hourly observations of conventional meteorological parameters, such as temperature, pressure, relative humidity, wind direction, and wind speed, were sourced from the European Centre for Medium-Range Weather Forecasts (ECMWF).

2.2 Box model simulation

This study employed an observation-constrained zero-dimensional photochemical reaction model (Observed 0-D box model) to simulate atmospheric photochemical processes. The chemical mechanism module is the core of the box model, and most mainstream studies use the Master Chemical Mechanism (MCM) nested within the model, incorporating processes such as solar radiation, boundary layer height, atmospheric photochemistry, and dry deposition (Zhang et al., 2022). The OBM model used in this study is AtChem2 (<https://atchem.leeds.ac.uk/webapp/>), which is equipped with the Master Chemical Mechanism (MCM v3.3.1: <https://mcm.york.ac.uk/MCM>) to simulate O_3 and radical chemistry and analyze their budgets (Wang et al., 2022a; Sommariva et al., 2020). The model includes approximately 143 VOCs, 6,700 chemical species, and over 17,000 reactions. Hourly resolution observational data of O_3 , NO, NO_2 , CO, SO_2 , HONO, VOCs (in total 82 species), meteorological parameters (e.g., temperature, relative humidity, pressure, and boundary layer height), and photolysis rates were used as model constraints. Photolysis rates for unmeasured species were calculated using the Tropospheric Ultraviolet and Visible Radiation Model (TUV v5.3) (Table S2). Additionally, to avoid unreasonable increases in the concentrations of constrained species, a dilution rate of $1/86400 \text{ s}^{-1}$ was applied. Before the simulation, the model underwent a 48-hour pre-run to stabilize unmeasured species (e.g., radicals).

The configuration of model mechanisms was informed by previous research, with a particular focus on the dry deposition processes of key species (e.g., O_3 , NO_2 , SO_2 , H_2O_2 , HNO_3 , PAN, and HCHO), the heterogeneous uptake reactions of HO_2 and N_2O_5 , and the $Cl\cdot$ chemistry mechanism. Dry deposition is a critical pathway for the transfer of atmospheric pollutants from



the gas phase to the Earth's surface, significantly influencing the concentration distribution and removal of regional pollutants. Many models have already incorporated this atmospheric physical process (Ma et al., 2022; Chen et al., 2020a). The heterogeneous uptake of HO₂, as an important sink, contributes to approximately 10 %–40 % of the global HO₂ concentration (Li et al., 2019). Studies have shown that including the heterogeneous uptake mechanism of HO₂ in simulations reduces P(O₃)_{net} concentration and alters the sensitivity to VOCs (Zhou et al., 2021; Dyson et al., 2022). Additionally, Cl[·] enhances atmospheric oxidation, accelerating the OH-HO₂-RO₂ reaction cycle (Ma et al., 2023). By incorporating these mechanisms, this study aims to more accurately simulate the atmospheric chemical processes and their impacts on pollutant concentrations in the PRD region (Zhou et al., 2024a). The configurations of each scenario are as follows: Case A considers only the simplified chemical reaction mechanism from the MCM, excluding dry deposition and heterogeneous reactions; Case B incorporates the HO₂ uptake by ambient aerosols mechanism based on Case A; Case C further includes the dry deposition processes of key species on top of Case B; and Case D₁ extends Case C by adding the N₂O₅ uptake mechanism and Cl[·] related heterogeneous reaction mechanisms. Detailed simulation parameter settings are provided in the supplementary information (Table S3).

175 2.3 Model performance evaluation

The Index of Agreement (IOA) was used to evaluate the simulation performance (Li et al., 2021).

$$IOA = 1 - \frac{\sum_{i=1}^n (O_i - S_i)^2}{\sum_{i=1}^n (|O_i - \bar{O}| - |S_i - \bar{O}|)^2} \quad (7)$$

where O_i and S_i represent the observed and simulated values, respectively, \bar{O} denote the mean of the observed values, and n is the number of samples. The IOA ranges from 0 to 1, with higher values indicating better agreement between observed and simulated values. In addition to the IOA, the Pearson correlation coefficient (R), mean bias (MB), normalized mean bias (NMB), root mean square error (RMSE), mean fractional bias (MFB) and mean fractional error (MFE) were used to evaluate the consistency between observed and simulated values (Table S7).

2.4 k_{OH}

Total OH reactivity (k_{OH}) is a crucial indicator of atmospheric chemical cycling and oxidative capacity (Gilman et al., 185 2009). k_{OH} is defined as the sum of the products of the concentrations of all reactive species X_i that can react with OH radicals and their respective reaction rate constants, calculated as follows:

$$k_{OH} = \sum_i k_{OH+X_i} \cdot [X_i] \quad (8)$$

where X_i includes CO, NO_x, and VOCs, among others, and k_{OH+X_i} is the reaction rate constant (s⁻¹) between reactive species X_i and OH radicals.

190 2.5 OFP

O₃ Formation Potential (OFP) is an indicator used to measure the relative contribution of different VOC species to ground-



level O₃ formation (Wu et al., 2020). The formula for OFP is as follows:

$$\text{OFP} = [\text{VOCs}]_i \times \text{MIR}_i \quad (9)$$

where [VOCs]_{*i*} represents the concentration of a specific VOC species *i* (μg m⁻³), and MIR represents the maximum incremental reactivity of the VOC species *i* (go₃/gvoc). MIR is used to characterize the increase in O₃ production per unit increase in VOCs under conditions where O₃ formation is most sensitive to VOCs.

2.6 Absolute $P(\text{O}_3)_{\text{net}}$ sensitivity

We calculated the modelled OFS using the absolute $P(\text{O}_3)_{\text{net}}$ sensitivity method from Sakamoto et al. (2019). It is defined as the change in $P(\text{O}_3)_{\text{net}}$ induced by a percentage increase in O₃ precursors. This method facilitates the quantitative assessment of how reductions in O₃ precursors contribute to the overall reduction of $P(\text{O}_3)_{\text{net}}$ over a period or within a region. The formula is as follows:

$$\text{Absolute } P(\text{O}_3)_{\text{net}} = \frac{\delta P(\text{O}_3)}{\delta \ln[X]} = P(\text{O}_3) \frac{\delta P(\text{O}_3)}{\delta \ln[X]} \quad (10)$$

In the equation, [X] represents NOx or VOCs. A positive absolute $P(\text{O}_3)_{\text{net}}$ sensitivity indicates that reducing the precursor will lead to a decrease in the $P(\text{O}_3)_{\text{net}}$. In contrast, a negative value indicates that reducing the precursor will lead to an increase in the $P(\text{O}_3)_{\text{net}}$ (Dyson et al., 2022). In this study, the analysis of absolute $P(\text{O}_3)_{\text{net}}$ sensitivity was conducted using the box model. Specifically, the model was used to calculate $P(\text{O}_3)_{\text{net}}$ and simulate the input precursor concentrations. The above formula was then applied to compute the simulated absolute $P(\text{O}_3)_{\text{net}}$ sensitivity, which was subsequently compared with the measured OFS results.

3 Results and discussion

210 3.1 Overview of observation campaign

The supplementary materials (Fig. S3, S4, and Table S4, S5) provide the time series plots, diurnal variation, and daytime averages (daytime: 6:00–18:00) of meteorological parameters, conventional pollutants, photolysis rate constants, NO, $P(\text{O}_3)_{\text{net}}$ and hourly VOCs concentrations from 4–26 October 2023, at the Guangdong Atmospheric Supersite of China. The site was located downwind of the Guangzhou-Foshan area, with atmospheric pollutants primarily originating from the northeast. To 215 access daily O₃ pollution levels, the maximum daily 8-hour average O₃ concentration (MDA8) was employed, in accordance with the Technical Specification for Ambient Air Quality Evaluation (Trial) (HJ 663-2013). In this study, days with MDA8-O₃ concentration exceeding the Class II limit stipulated by the Ambient Air Quality Standards (GB3095-2012) were defined as O₃ pollution days (with MDA8-O₃ concentration limit of 160 μg m⁻³ (equivalent to approximately 81.6 ppbv at 25°C), while others were defined as normal days.

220 During the whole observation period, there were 6 O₃ pollution days (15–17 and 24–26 October 2023). The maximum O₃ mixing ratio (136.5 ppbv) occurred at 15:00 on 25 October 2023, while the maximum $P(\text{O}_3)_{\text{net}}$ (53.7 ppbv h⁻¹) occurred at



10:00 on 24 October 2023. Diurnal variation plots show that O_3 and $P(O_3)_{net}$ exhibited single-peak patterns, with O_3 peaking at 15:00 and $P(O_3)_{net}$ peaking between 9:00-10:00. On O_3 pollution days, the daytime average concentrations of O_3 and $P(O_3)_{net}$ during the observation period were 63.2 ± 37.6 ppbv and 14.4 ± 13.8 ppbv h^{-1} , respectively, both approximately twice as high as on normal days (daytime average O_3 : 30.9 ± 22.9 ppbv; daytime average $P(O_3)_{net}$: 7.2 ± 9.4 ppbv h^{-1}). The maximum values of directly measured $P(O_3)_{net}$ in different ambient environments in previous studies are listed in Table S6, ranging from 10.5 to 100 ppbv h^{-1} , and the measured $P(O_3)_{net}$ values in this study fall within this range, demonstrating the reasonableness of the values measured in this study.

As shown in Fig. S4, the diurnal variation of parameters on O_3 pollution days and normal days indicates that the nighttime background concentrations of O_3 precursors (TVOC and NO_x) are higher on O_3 pollution days. However, during the period of strongest sunlight (11:00-14:00), the concentrations of TVOC and NO_x on O_3 pollution days are lower than those on normal days. Specifically, on O_3 pollution days, the TVOC concentration is $11.4 \mu\text{g m}^{-3}$, and the NO_x concentration is 13.5 ppbv, while on normal days, the TVOC concentration is $13.7 \mu\text{g m}^{-3}$, and the NO_x concentration is 14.8 ppbv. This suggests that stronger photochemical reactions occur on O_3 pollution days, leading to lower daytime concentrations of precursors compared to normal days. The diurnal variation of NO concentration on O_3 pollution days showed an early morning peak at 8:00, rising to 12.2 ppbv and then decreasing to 1.6 ppbv. By comparing the diurnal variation data between O_3 pollution days and normal days, we found that both O_3 concentrations and $P(O_3)_{net}$ values were significantly higher on O_3 pollution days, particularly during the daytime (6:00-18:00). This phenomenon aligns with the conclusion that high temperatures, low humidity, strong radiation, and stable weather conditions favor O_3 pollution formation.

240 3.2 Characteristics of VOC concentrations and composition

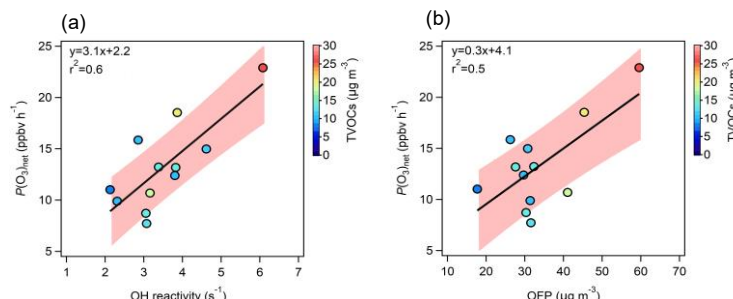
This study analyzed 110 VOC species, examining the contributions of different categories to TVOC concentrations, k_{OH} , and daily OFP. We also identified the top 10 VOC species contributing to these three indicators (Fig. S5), aiming to explore the atmospheric presence, chemical reactivity, and environmental impact of VOCs. Additionally, this study used two classification methods to group VOC species. Method 1 divided VOCs into alkynes (1 species), alkanes (27 species), alkenes (11 species), aromatic hydrocarbons (17 species), OVOCs (20 species), halogenated hydrocarbons (33 species), and sulfur-containing VOCs (1 species). Method 2 categorized VOCs into BVOC (Biogenic Volatile Organic Compounds), OVOCs (Oxygenated Volatile Organic Compounds), and AVOCs/NMHC (Anthropogenic Volatile Organic Compounds), with specific classifications shown in Table S4.

During the observation period, the daily average TVOC concentration ranged from 7.2 to $28.9 \mu\text{g m}^{-3}$. OVOCs contributed the most (40.8 %), followed by halogenated hydrocarbons (20.8 %), aromatic hydrocarbons (18.3 %), alkanes (17.9 %), alkenes (1.7 %), and alkynes (0.5 %). The k_{OH} average value was $12.1 \pm 3.9 \text{ s}^{-1}$, primarily contributed by OVOCs (62.9 %), followed by halogenated hydrocarbons (10.8 %), alkenes (10.4 %), aromatic hydrocarbons (9.8 %), alkanes (6.0 %), and alkynes (0.1 %). Among the alkenes in the known MCM mechanism, ethylene, as an indicator of VOCs, had the highest



proportion, accounting for 10.7 % of alkenes k_{OH} and 2.8 % of NMHC k_{OH} . Formaldehyde, another VOCs indicator, was the
255 most dominant species in OVOCs k_{OH} , contributing about 13.3 %. Among VOC species, OVOCs contributed the most to OFP (51.6 %), followed by aromatic hydrocarbons (32.9 %), alkenes (8.0 %), alkanes (6.9 %), halogenated hydrocarbons (0.5 %), and alkynes (0.2 %). The analysis results show that although halogenated hydrocarbons dominate VOCs concentration emissions, their contribution to O_3 pollution is low. In contrast, alkenes, despite their lower contribution to VOCs concentration emissions, are important precursors for O_3 formation. Based on the comprehensive analysis of VOCs concentration, k_{OH} , and
260 OFP, OVOCs and aromatic hydrocarbons significantly contribute to O_3 formation and should be prioritized as key VOC species for O_3 pollution control in the PRD region. This result aligns with other related studies in the PRD, such as those in Shenzhen (Yu et al., 2020; Guanghe et al., 2022), Guangzhou (Pei et al., 2022), and Jiangmen (Jing et al., 2024), which indicate that OVOCs and aromatic hydrocarbons are key VOC species for O_3 formation.

Overall, toluene, m/p-xylene, formaldehyde, 2-hexanone, ethyl acetate, and tetrahydrofuran consistently ranked in the top
265 10 VOC species in terms of concentration, k_{OH} and OFP contribution. These VOC species mainly originate from human activities, such as industrial production, solvent use, traffic emissions, and fuel combustion, highlighting the significant impact of anthropogenic sources on O_3 pollution (Cai et al., 2010; Yang et al., 2023; Zheng et al., 2019).



270 **Figure 1: Correlation between measured $P(\text{O}_3)_{\text{net}}$ ($P(\text{O}_3)_{\text{net}}\text{ Mea}$) and (a) total OH reactivity (k_{OH}) and (b) O_3 Formation Potential (OFP).**

Figure 1 shows the correlation between $P(\text{O}_3)_{\text{net}}\text{ Mea}$ and k_{OH} and OFP (calculated using the daytime average data during
275 the observation period). The shaded area in the figure represents the confidence interval (68.3 %) of the fitting line between $P(\text{O}_3)_{\text{net}}$ and k_{OH} , and between $P(\text{O}_3)_{\text{net}}$ and OFP. Data outside the confidence interval may be due to the fact that the calculation of k_{OH} and OFP did not fully consider the environmental conditions and atmospheric chemistry complexity at the observation site (Zhang et al., 2024; Yadav et al., 2024). The color of the scatter points represents the TVOC concentration. The r^2 values between $P(\text{O}_3)_{\text{net}}$ measurements and k_{OH} and OFP are 0.6 and 0.5, respectively, indicating that VOCs with higher k_{OH} and OFP significantly enhance the $P(\text{O}_3)_{\text{net}}$.

3.3 Comparison and optimization of simulated and measured $P(\text{O}_3)_{\text{net}}$ values

285 Based on our previous research (Zhou et al., 2024a), we named the scenario considering only the current chemical reaction mechanism from the MCM v3.3.1 in the box model as Case A. Subsequently, we gradually incorporated the HO_2 uptake by



ambient aerosols, dry deposition, N_2O_5 uptake, and ClNO_2 photolysis mechanisms into the MCM mechanism in the box model, implemented as modelling scenarios labeled Case B, Case C, and Case D₁. The specific parameter settings for each scenario are shown in Table S3. The time series and diurnal variations of the $P(\text{O}_3)_{\text{net_Mea}}$ and $P(\text{O}_3)_{\text{net_Mod}}$ for Cases A–D₁ are shown in Fig. S7. To evaluate the model's performance, $P(\text{O}_3)_{\text{net_Mea}}$ and $P(\text{O}_3)_{\text{net_Mod}}$ data were used to calculate the IOA, R, MB, NMB, RMSE, MFB and MFE values to access the model's performance under different scenarios (Table S7). The IOA values between $P(\text{O}_3)_{\text{net_Mod}}$ and $P(\text{O}_3)_{\text{net_Mea}}$ were all > 0.86 , and R ranged from 0.84–0.98, indicating that the model can reasonably reproduce the changes in $P(\text{O}_3)_{\text{net}}$. However, the MB and NMB were $-3.0\text{--}2.4 \text{ ppbv h}^{-1}$ and $-30.5\text{--}24.9 \text{ %}$, respectively, indicating a systematic underestimation of $P(\text{O}_3)_{\text{net}}$. The RMSE ranged from 7.0 to 7.2 ppbv h^{-1} , while the MFB and MFE were $-3.1\text{--}1.7 \text{ %}$ and $53.8\text{--}55.5 \text{ %}$, respectively. These results suggest that while the model captures the overall trends well, there is room for improvement in reducing simulation biases.

In all modelling scenarios from Case A–Case D₁, $P(\text{O}_3)_{\text{net_Mod}}$ values were generally lower than $P(\text{O}_3)_{\text{net_Mea}}$. Although the correlation between $P(\text{O}_3)_{\text{net_Mea}}$ and $P(\text{O}_3)_{\text{net_Mod}}$ was good (Fig. S9), even after incorporating mechanisms that may compensate for O_3 production simulation biases into to the box model (labeled as Case D₁), the simulated daytime average $P(\text{O}_3)_{\text{net_Mod}}$ was still 3.4 ppbv h^{-1} lower than $P(\text{O}_3)_{\text{net_Mea}}$ (26.3 % bias), with a peak deviation of up to 13.3 ppbv h^{-1} (44.8 %), as shown in Fig. 2. we defined the difference between $P(\text{O}_3)_{\text{net_Mea}}$ and $P(\text{O}_3)_{\text{net_Mod}}$ as $P(\text{O}_3)_{\text{net_Missing}}$, and its time series is shown in Fig. S10. During the observation period, 7–10 October and 18–22 October were rainy days, with a median $P(\text{O}_3)_{\text{net_Missing}} < 1.1 \text{ ppbv h}^{-1}$; therefore, these days were excluded when calculating the diurnal variations of different O_3 production and consumption pathways. On non-rainy days, the median $P(\text{O}_3)_{\text{net_Missing}}$ was $4.9 \pm 4.1 \text{ ppbv h}^{-1}$, with the peak median $P(\text{O}_3)_{\text{net_Missing}}$ reaching 17.5 ppbv h^{-1} on 15 October 2023. The median $P(\text{O}_3)_{\text{net_Missing}}$ values on O_3 pollution days were statistically higher than those on normal days (*t*-test, $P < 0.5$), indicating that the supplementary mechanisms explored in the model, as mentioned above, are not the main cause of the $P(\text{O}_3)_{\text{net_Missing}}$.

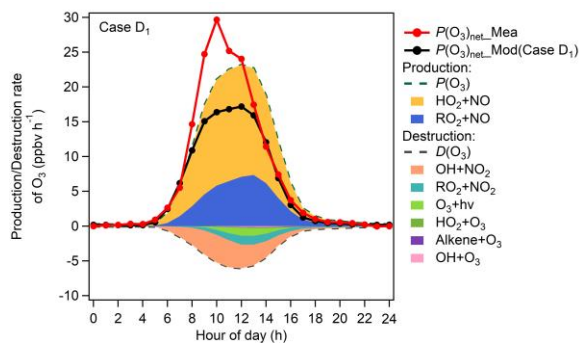


Figure 2: Diurnal variations (excludes rainy days) of O_3 production and destruction rates modelled in Case D₁, and measured ($P(\text{O}_3)_{\text{net_Mea}}$) and modelled ($P(\text{O}_3)_{\text{net_Mod}}$) $P(\text{O}_3)_{\text{net}}$.

We further explore the possible reasons for the discrepancies between $P(\text{O}_3)_{\text{net_Mea}}$ and $P(\text{O}_3)_{\text{net_Mod}}$ using the modelling results of Case D₁. The ratio of cumulative $P(\text{O}_3)_{\text{net_Mea}}$ and $P(\text{O}_3)_{\text{net_Mod}}$ derived from Case D₁ was 1.4, calculated by summing the daytime data with 1 h resolution during the observation period. This result is close to the previous research



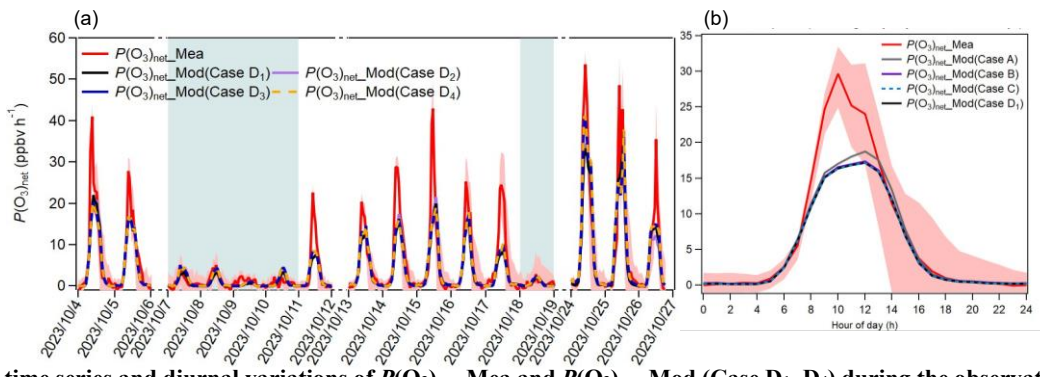
findings, such as Cazorla et al. reporting a ratio of 1.3 (Cazorla and Brune, 2009), Ren et al. (2013) and Hao et al. (2023) reporting a ratio of 1.4. As shown in Fig. 2, we found that the $\text{HO}_2 + \text{NO}$ reaction dominated the O_3 production process, accounting for 71.4 % of total O_3 production pathways. In contrast, the main pathways for O_3 consumption were $\text{OH} + \text{NO}_2$ and $\text{RO}_2 + \text{NO}_2$, accounting for 67.9 % and 16.5 % of total O_3 consumption pathways, respectively. The importance of the HO_2/RO_2 reaction pathways indicates that simulation biases in HO_2/RO_2 can further affect the accuracy of $P(\text{O}_3)_{\text{net_Mod}}$.

To further investigate the causes of $P(\text{O}_3)_{\text{net_Missing}}$, we conducted correlation analyses between $P(\text{O}_3)_{\text{net_Missing}}$ and parameters such as TVOC, NO_x , J_{O_3} , T and O_x under both O_3 pollution days and normal days; the results are shown in Fig. S11. Under O_3 pollution days, $P(\text{O}_3)_{\text{net_Missing}}$ showed a positive correlation with VOCs and NO_x , with r^2 values of 0.4 and 0.5, respectively, indicating that $P(\text{O}_3)_{\text{net_Missing}}$ increases significantly at higher O_3 precursor concentrations. This phenomenon is consistent with previous studies (Whalley et al., 2021; Ren et al., 2013; Zhou et al., 2024a). Meanwhile, $P(\text{O}_3)_{\text{net_Missing}}$ exhibited a positive correlation with J_{O_3} on both O_3 pollution days and normal days, with r^2 values of 0.5 and 0.4, respectively. In contrast, $P(\text{O}_3)_{\text{net_Missing}}$ showed no significant correlation with TVOC, NO_x , T , or O_x under normal days ($r^2 < 0.2$). This suggests that $P(\text{O}_3)_{\text{net_Missing}}$ may be related to the missing mechanisms for photolabile unknown VOCs in the box model. Research by Wang et al. (2022b) indicates that constraining OVOCs in the model is crucial for the accuracy of $P(\text{O}_3)_{\text{net_Mod}}$, and photochemical models without OVOCs constraints significantly underestimate $P(\text{O}_3)_{\text{net}}$. In our previous study on the industrial city of Dongguan (Zhou et al., 2024b), we used parameter equations developed by Wang et al. (2024a; 2024b) to quantify the impact of missing k_{OH} on $P(\text{O}_3)_{\text{net_Missing}}$ and qualitatively tested the potential compensating effects of unmeasured acetaldehyde, acrolein, acetone, butanone, and branched alkenes in Dongguan on $P(\text{O}_3)_{\text{net_Missing}}$. Compared to the campaign conducted in Dongguan (Zhou et al., 2024a), this study measured more VOC species (Table S4). Therefore, we further compensate for the Case D₁ scenario by constraining more measured VOC species compared to the study in Dongguan (e.g., OVOCs, halogenated hydrocarbons) to explore their impact on $P(\text{O}_3)_{\text{net_Mod}}$. The specific simulation scenario settings are described in Table S3.

Figure 3 shows the time series and diurnal variations of $P(\text{O}_3)_{\text{net_Mea}}$ and $P(\text{O}_3)_{\text{net_Mod}}$ (under Case D₁–D₄) during the observation period. Specifically, we added constraints for measured acetaldehyde, acrolein, acetone, and butanone (OVOCs, which were considered as potential contributors for $P(\text{O}_3)_{\text{net_Missing}}$ in Dongguan in our previous study, Zhou et al., 2024) to the model based on Case D₁, which is labeled as Case D₂. However, the daytime average value of $P(\text{O}_3)_{\text{net_Mod}}$ from Case D₂ increased by only 0.5 % compared to Case D₁, this indicates that the dominant OVOCs species that causes $P(\text{O}_3)_{\text{net_Missing}}$ may vary between Heshan and Dongguan. We further constrained all measured OVOC species in Heshan (which included additional OVOCs species compared to that added to Case D₂, such as propionaldehyde, butyraldehyde, and valeraldehyde) that could be input into the box model in the Case D₃ simulation scenario (more details can be found in Table S8). The results showed that the averaged daytime $P(\text{O}_3)_{\text{net_Mod}}$ from Case D₃ increased by 4.4 % compared to that in Case D₂. Notably, in Case D₃, constraining all OVOC species significantly improved $P(\text{O}_3)_{\text{net_Mod}}$ during the morning period (8:00–9:00), with an increasing rate of approximately 10.2 % ($\sim 1.3 \text{ ppbv h}^{-1}$). Additionally, Case D₄ scenario added constraints for chlorine-containing VOCs (i.e., all measured VOC species listed in Table S8 that could be input into the OBM model were constrained).



355 The daytime average $P(O_3)_{net_Mod}$ values from Case D₄ changed by only 1.1 % compared to those derived from Case D₃, indicating that the potential contribution of OVOCs to compensating $P(O_3)_{net_Missing}$ is greater than that of chlorine-containing VOCs. However, in modelling scenario Case D₄, the daytime average $P(O_3)_{net_Mod}$ still showed a 22.2 % underestimation compared to the measured values.



360 **Figure 3: The time series and diurnal variations of $P(O_3)_{net_Mea}$ and $P(O_3)_{net_Mod}$ (Case D₁–D₄) during the observation period. The**
365 **shaded areas in (a) represent rainy days.**

370 The diurnal variations of O₃ production pathways in Case D₄ are shown in Fig. S12. Compared to Case D₁, the RO₂+NO reaction rate in Case D₄ was higher by 0–2.1 ppbv h⁻¹ in the diurnal variations during the whole measurement period (excluded the rainy days). The RO₂ species with higher contributions to this pathway included CH₃O₂, HO₂C₄O₂, HO₁₃C₄O₂, HOCH₂CH₂O₂, HO₃C₄O₂, CH₃COCH₂O₂, and COCCOH₂CO₂. This indicates that the constraints on additional OVOCs in Case D₄ (such as aldehyde and ketone compounds with specific functional groups, e.g., carbonyl and hydroxyl) increased the intermediate RO₂ products, leading to a significant enhancement in the RO₂+NO reaction rate. This suggests their large potential to contribute to $P(O_3)_{net_Missing}$.

375 The modelling results of scenarios Case D₁–D₄ show that although constraining the measured VOC species in the box model mechanism can reduce $P(O_3)_{net_Missing}$ to some extent, there is still a significant gap between the simulated and measured $P(O_3)_{net}$ values. Therefore, the potential contribution of unmeasured VOC species to compensating $P(O_3)_{net_Missing}$ in the box model mechanism cannot be ignored. Yang et al. (2017) and Tan et al. (2019) conducted radical measurements at 380 the Guangdong Atmospheric Supersite of China in autumn of 2014, revealing missing k_{OH} contributions of approximately 32 % and 50 %, respectively. Yang et al. (2017) pointed out that the missing k_{OH} contributions in the Heshan region may originate from OVOCs such as aldehydes, acids, and dicarbonyls. Tan et al. (2019) indicated that about 60 % of the O₃ produced in the Heshan region was contributed by unmeasured VOCs. We hypothesize that the remaining $P(O_3)_{net_Missing}$ is caused by unknown VOCs that are not constrained in the box model. By quantifying the relationship between k_{OH} and $P(O_3)_{net}$, the contribution of missing k_{OH} ($k_{OH_Missing}$) to $P(O_3)_{net_Missing}$ can be assessed, and compensating for $k_{OH_Missing}$ in the box model can help reduce $P(O_3)_{net_Missing}$. Figure 4 shows the relationship between k_{OH} and $P(O_3)_{net_Mod}$ calculated under the Case D₁ scenario, which can be expressed as:

$$P(O_3)_{net_Missing} = 3.4 \times k_{OH_Missing} - 2.7 \quad (11)$$

where $P(O_3)_{\text{net}}$ and k_{OH} in the equation represent the daytime averaged values for each day. Based on this relationship, we calculated k_{OH} according to calculated $P(O_3)_{\text{net}}$ for each day. This value was then used to compensate for the unmeasured VOCs in the model (with a daytime k_{OH} compensation range of 1.2–2.4 s^{-1}). Based on the significant contribution of OVOCs to $P(O_3)_{\text{net}}$ mentioned earlier, we designed three modelling scenarios to compensate for k_{OH} , with the specific multiples varying each day: (1) Case E₁: by expanding the constrained overall VOCs concentrations in Case D₁, the daily TVOC concentration was increased by 1.1 to 1.7 times; (2) Case E₂: according to k_{OH} ratio of NMHC to OVOCs in the constrained VOCs of Case D₁, the concentrations of ethylene (a representative NMHC species) and formaldehyde (OVOCs indicator) were expanded separately. The ethylene concentration was increased by 5.9 to 85.6 times, and the formaldehyde concentration was increased by 1.4 to 2.0 times; (3) Case E₃: by expanding only the formaldehyde concentration to compensate for k_{OH} , in this case, the daily formaldehyde concentration was increased by 1.8 to 9.2 times, to verify the role of OVOCs in compensating for $P(O_3)_{\text{net}}$.

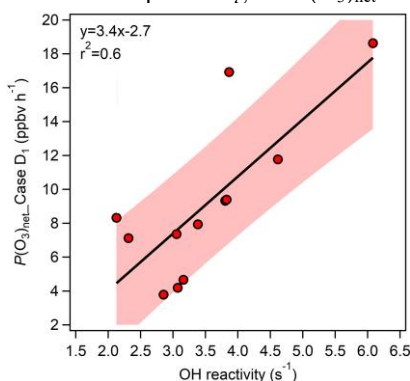


Figure 4: The relationship between k_{OH} and $P(O_3)_{net_Mod}$ calculated under the Case D1 scenario (using the daily daytime average values during the observation period).

410 In Case E₁, where the overall TVOC concentration was increased to compensate for k_{OH} Missing without distinguishing VOCs categories, the compensation effect was limited due to the dilution effect of low-reactivity VOCs, resulting in a reduction of the daytime average $P(O_3)_{net}$ Missing proportion from 26.3 % (calculated as $P(O_3)_{net}$ Missing/ $P(O_3)_{net}$ Mea) to 10.3 %. In Case E₂, where the concentrations of ethylene and formaldehyde were expanded, the daytime average $P(O_3)_{net}$ Missing proportion reduced from 26.3 % to 17.2 %. This proportion is higher than that obtained from Case E1, which may be due to the relatively low reactivity of ethylene limited the overall compensation effect. In contrast, Case E₃ compensated for k_{OH} Missing solely by expanding the formaldehyde concentration. Since formaldehyde, as a representative high-reactivity OVOC species, contributes more directly and significantly to O₃ generation through photochemical pathways (Mousavinezhad et al., 2021), it achieved the best compensation effect, reducing the daytime average of $P(O_3)_{net}$ Missing from 26.3 % to 5.1 %. However, $P(O_3)_{net}$ Missing during the peak period of diurnal variation remained at 9.0 ppbv h⁻¹. This result confirms the critical role of high-reactivity OVOCs (especially those with the same photochemical reaction characteristics as formaldehyde) in compensating for $P(O_3)_{net}$ Missing. Further, it suggests the potential presence of other unmeasured high-reactivity VOC species in the ambient atmosphere. Constraining these species could help further improve the model's simulation accuracy (Lyu et al.,



2024; Wang et al., 2024b). Overall, the degree of compensation for $P(O_3)_{\text{net_Missing}}$ follows the order Case E₃>Case E₁>Case E₂, which may be related to the reactivity of the selected VOCs.

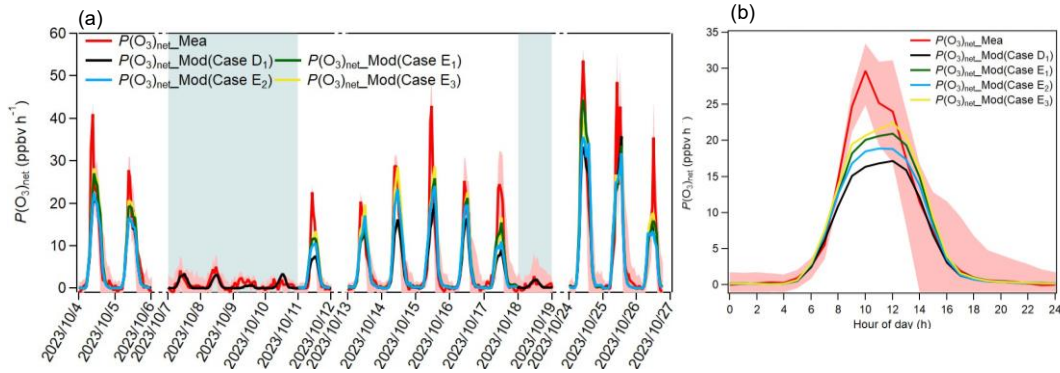


Figure 5: (a) Time series and (b) diurnal variations of $P(O_3)_{\text{net_Mea}}$ and $P(O_3)_{\text{net_Mod}}$ (Case D₁–E₃) during the observation period; (b) Diurnal variations excluding rainy days. The shaded areas in (a) represent rainy days.

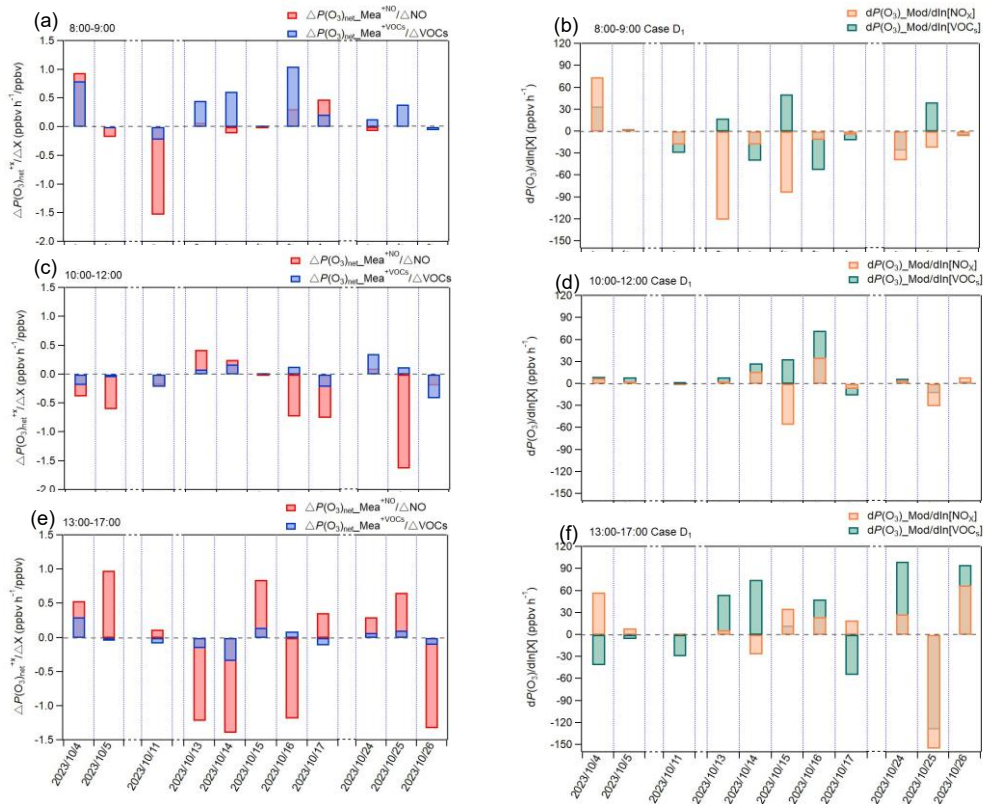
4. OFS assessment based on measurements and simulations

This study systematically estimated OFS during the observation period (4–5, 11, 13–17, and 24–26 October 2023) using measured OFS (more details see Sect. 2.1) and modelled OFS (more details are shown in Sect. 2.6). Fig. S14 presents the diurnal variations of the directly measured IR index from OFS experiments, as well as the absolute $P(O_3)_{\text{net}}$ sensitivity of NO_x and VOCs calculated based on the box model (Case D₁, Eq. (9)). We see from Fig. S14 that both measured OFS and modelled OFS captured the same diurnal OFS trend: an early morning (8:00–12:00) VOCs-limited/transition regime shifting to a NO_x-limited regime around midday (13:00), followed by a return to VOCs-limited/transition conditions in the afternoon (14:00–18:00). This midday transition to NO_x-limited conditions is chemically reasonable, where intensified NO₂ photolysis boosts Ox production while concurrently diminished NO titration and declining VOCs emissions collectively favor NO_x-sensitive chemistry during peak sunlight hours (Wang et al., 2023). The overall OFS classification (mainly VOCs-limited and transition regimes) aligns with previous studies in Guangdong in autumn (Song et al., 2022; Chen et al., 2020b; Wu et al., 2020; Jing et al., 2024). However, the OFS assessment results from measured and modelling methods showed only 60 % agreement in hourly OFS variations (see Fig. S14).

In order to gain a deeper understanding of the similarities and differences between the direct measurement and the model simulation methods in diagnosing OFS, we divided the daytime observation period into three characteristic phases: the $P(O_3)_{\text{net}}$ rising phase (8:00–9:00), the $P(O_3)_{\text{net}}$ stable phase (10:00–12:00), and the $P(O_3)_{\text{net}}$ declining phase (13:00–17:00). Fig. 6 (a), (c), and (e) present the diurnal cumulative average results of IR derived from direct measurements of $\Delta P(O_3)_{\text{net}}^{+NO}$ and $\Delta P(O_3)_{\text{net}}^{+VOCs}$ using the NPOPR detection system for each phase. Fig. 6 (b), (d), and (f) show the diurnal cumulative average results of the absolute $P(O_3)_{\text{net}}$ sensitivity calculated from the box model (Case D₁) for each phase. We found that during $P(O_3)_{\text{net}}$ rising phase, both the direct measurement method and the model simulation method identified the OFS as being in the transition regime or VOCs-limited regime. However, the agreement between these two methods was only 63.6 %. This low consistency may be related to the rapid changes in precursor concentrations in the morning: the concentrations of VOCs and



NO_x change quickly during this period, particularly due to traffic emissions and industrial activities, and these rapid variations in precursor concentrations make it challenging for the model to accurately capture the instantaneous reaction dynamics (Cao et al., 2021). During the $P(O_3)_{net}$ stable phase, the consistency between these two methods improved significantly, reaching an agreement of 72.7 %, with the OFS mostly located in the transition regime. This higher consistency occurred during periods of higher solar radiation intensity, when photochemical reactions were more stable. This stability resulted in improved model simulation accuracy. In the $P(O_3)_{net}$ declining phase, the OFS assessment results between these two methods researching an agreement of 72.7 %, both methods predominantly identified the OFS as either the transition regime or NO_x-limited regime. This relatively high agreement may be attributed to the reduced intensity of solar radiation and the decreased complexity of photochemical reactions in the afternoon, as Chen et al. (2025) showed that lower solar radiation simplifies reaction pathways, thereby enhancing model simulation accuracy.



485

Figure 6: Average values of IR derived from the direct measurement data using the NPOPR detection system (e.g., $\Delta P(O_3)_{net}^{+NO}$ and $\Delta P(O_3)_{net}^{+VOCs}$) and absolute $P(O_3)_{net}$ sensitivity from the box model during (a)–(b) $P(O_3)_{net}$ rising phase (8:00–9:00) ; (c)–(d) $P(O_3)_{net}$ stable phase (10:00–12:00) (e)–(f) $P(O_3)_{net}$ declining phase (13:00–17:00).

The absolute $P(O_3)_{net}$ sensitivity for scenarios Case E₁–Case E₃ are shown in Fig. S15. The agreement between these 490 scenarios and the direct measurement results changes across different periods, with consistency levels of 54.5–63.6 %, 45.5–



72.7 %, and 63.6–72.7 % during $P(O_3)_{net}$ rising phase, $P(O_3)_{net}$ stable phase, and $P(O_3)_{net}$ declining phase, respectively. In cases where $P(O_3)_{net_Missing}$ was reduced (Case E₁–Case E₃), the OFS sometimes shifted to NO_x-limited conditions during certain periods, such as in Case E₂ during the $P(O_3)_{net}$ rising phase and Case E₃ during the $P(O_3)_{net}$ stable phase on October 4, 2023. This contradictory phenomenon may be related to the model's incomplete representation of unknown high-reactivity VOCs chemical mechanisms (e.g., aldehyde and ketone). Additionally, previous studies have pointed out that the diagnostic method based on the box model tends to overestimate the sensitivity to VOCs in certain regions of China due to neglecting the reactivity of unidentified VOCs in anthropogenic emissions (Xu et al., 2022; Lu et al., 2010). To more accurately simulate O₃ formation and precursor sensitivity, Xu et al. (2022) incorporated formaldehyde as input data in the box model, and found that this improvement significantly reduced the model's bias in diagnosing OFS, particularly in misjudging the VOCs-limited regime.

It is noteworthy that there are differences in the precursor sensitivity response mechanisms between the absolute $P(O_3)_{net}$ sensitivity assessment method based on the box model and the direct measurement method. For example, during the $P(O_3)_{net}$ stable phase (10:00–12:00 period) on 4–5 October, although both methods identified the OFS as being in the transition regime, the direct measurement showed that an increase in precursor concentrations suppressed $P(O_3)_{net}$, while the model simulations indicated that a reduction in precursor concentrations led to a decrease in $P(O_3)_{net}$. However, these findings only explain regional differences in sensitivity determinations, and the underlying reasons for the differing precursor sensitivity response mechanisms between the two methods may require further investigation.

5 Conclusions

Understanding ozone (O₃) production mechanisms is critical for accurate O₃ pollution assessment and control, as photochemical production directly effects O₃ concentration levels. Due to the absence of certain mechanisms in conventional models, particularly the kinetics from missing reactive volatile organic compounds (VOCs) species, the reliability of net photochemical O₃ production rates ($P(O_3)_{net}$) and O₃ formation sensitivity (OFS) evaluation is compromised. To address this issue, we employed the developed $P(O_3)_{net}$ (NPOPR) detection system based on the dual-reaction chamber technique to measure the $P(O_3)_{net}$ and OFS. The system was applied in field observations at the Guangdong Atmospheric Supersite of China in Heshan, Pearl River Delta during the autumn of 2023. By combining the NPOPR detection system and the box model, a systematic investigation of $P(O_3)_{net}$ and OFS was carried out.

During the observation period (4–26 October 2023), a total of 6 O₃ pollution days were recorded, with the maximum O₃ mixing ratio reaching 136.5 ppbv. The $P(O_3)_{net}$ levels on O₃ pollution days were significantly higher than those on normal days, indicating that high temperatures, low humidity, strong solar radiation, and stagnant weather conditions favor the O₃ pollution formation (see Sect. 3.1). The observational results show that oxygenated volatile organic compounds (OVOCs) and aromatic hydrocarbons contributing 51.6 % and 32.9 % to OFP, respectively, which are the primary contributors to O₃ formation. These species are mainly emitted by anthropogenic emissions.

Systematic underestimation in the modelled $P(O_3)_{net}$ ($P(O_3)_{net_Mod}$) was found when compared to the measured ($P(O_3)_{net_Mea}$), which is defined as $P(O_3)_{net_Missing}$. In the Case A modelling, only the simplified chemical reaction



mechanism from the MCM was considered, and we see the daytime average $P(O_3)_{net_Missing}$ was around 2.6 ppbv h^{-1} (20.3 %),
525 After gradually incorporating mechanisms such as HO_2 uptake by ambient aerosols, dry deposition, N_2O_5 uptake, and ClNO_2 photolysis (Case D₁), these gaps didn't get filled. The daytime average $P(O_3)_{net_Missing}$ was 3.4 ppbv h^{-1} (26.3 % underestimation), with the highest daily median (50th percentile) attaining 17.5 ppbv h^{-1} on O_3 pollution days. After adding constraints for VOC species such as acetaldehyde, acrolein, acetone, and butanone compared to Case D₁ (defined as Case D₂), the $P(O_3)_{net_Mod}$ values increased by only 0.5 % compared to the modelling scenario Case D₁. However, after further 530 constraining all measurable OVOC species (Case D₃), the $P(O_3)_{net_Mod}$ values increased by 4.4 % compared to those obtained from Case D₂, with a notable improvement of 10.2 % (approximately 1.3 ppbv h^{-1}) during the $P(O_3)_{net}$ rising phase (8:00-9:00). This indicates that OVOCs play a particularly significant role in O_3 formation during the morning. Additionally, after adding chlorine-containing VOCs (in Case D₄), the $P(O_3)_{net_Mod}$ values increased by only 1.1 % compared to those obtained from Case D₃, further confirming the dominant role of OVOCs in compensating for $P(O_3)_{net_Missing}$. These results also demonstrate 535 that by adding some missing mechanisms and measured VOCs species cannot fully eliminate simulation biases.

Further analysis revealed that unmeasured VOCs, especially OVOCs, are the primary cause of these deviations. To quantify this effect, we developed a compensation approach based on the observed relationship between daytime averages $P(O_3)_{net_Missing}$ and $k_{OH_Missing}$. This approach hypothesized that upscaling measured VOCs could compensate for $k_{OH_Missing}$ attributed to unmeasured species, thereby reducing $P(O_3)_{net_Missing}$. Building upon Case D₁, designed three 540 modelling scenarios (Case E₁: expanded TVOC; Case E₂: expanded ethylene and formaldehyde; Case E₃: expanded formaldehyde) to compensate for $P(O_3)_{net_Missing}$. Among these modelling scenarios, the daytime average $P(O_3)_{net_Missing}$ of Case E₁, Case E₂, and Case E₃ reduced to 10.3 %, 17.2 %, and 5.1 %, respectively. Notably, Case E₃ achieved the most significant reduction by solely increasing formaldehyde concentrations, validating the critical role of highly reactive OVOCs (particularly formaldehyde) in compensating for $P(O_3)_{net_Missing}$. This suggests that there may be other unmeasured highly reactive VOC species in the ambient atmosphere, and constraining these species could further improve the model's simulation accuracy.

Additionally, the sensitivity assessment results derived from the different measured and modelled OFS approaches were compared: (1) in direct measurement using the NPOPR detection system, NO or VOCs were added to quantify changes in $P(O_3)_{net}$, with OFS determined through the incremental reactivity (IR) index ($IR = \Delta P(O_3)_{net}^{+x} / \Delta S(x)$, where X = NOx or VOCs and $\Delta S(x)$ represents the added concentration); (2) in model simulations, where the box model calculated $P(O_3)_{net}$ and derived absolute $P(O_3)_{net}$ sensitivity ($\delta P(O_3)_{net} / \delta [X]$, where X = NOx or VOCs). Meanwhile we found that the agreement of OFS 550 assessment results between the direct measurements and the model results was lower in the $P(O_3)_{net}$ rising phase (8:00-9:00, 63.6 %) than those in the $P(O_3)_{net}$ stable phase (10:00-12:00, 72.7 %) and $P(O_3)_{net}$ declining phase (13:00-17:00, 72.7 %). This again highlights the importance of highly reactive OVOCs in improving the accuracy of OFS assessment. These results indicate that reducing $P(O_3)_{net_Missing}$ can enhance the accuracy of OFS assessment to some extent, but fully eliminating the discrepancies still requires further constraints on unmeasured VOC species and further research.

In conclusion, improving the model's accuracy requires further expansion of the measurement of VOC species,



particularly OVOCs, and the incorporation of relevant chemical mechanisms into the model. In future studies, continuing field observations based on direct measurement of $P(O_3)_{net}$ and accumulating more data will contribute to a better understanding of
560 O_3 pollution formation mechanisms and make effective O_3 pollution control strategies.

Date availability. The datasets supporting this research are included in this manuscript and its supplementary information files. The data for this study are also publicly available at <https://doi.org/10.5281/zenodo.15052519>. Meteorological data were sourced from the European Centre for Medium-Range Weather Forecasts (ECMWF, <https://www.ecmwf.int/>). Box model simulations were conducted using the AtChem2 model (<https://atchem.leeds.ac.uk/webapp/>) with the Master Chemical Mechanism (MCM v3.3.1, <https://mcm.york.ac.uk/MCM>). Figures in this study were created using Igor Pro 6.7. Additional data or materials related to this study can be made available upon reasonable request to the corresponding author (junzhou@jnu.edu.cn), subject to restrictions on data resources.

Author contributions. Author contributions. JZ and MS designed this study. BZ and JZ wrote the manuscript with
570 contributions from all co-authors. BZ, JZ, TZ, DC, BJ, YZ, J. Li, MD, MX, JHJ, and J. Luo collected and analyzed the data. All authors reviewed and revised the manuscript.

Competing interests. The contact author has declared that none of the authors has any competing interests.

Acknowledgments. Many thanks to the Guangdong Ecological and Environmental Monitoring Center.

Financial support. This work was funded by the National Natural Science Foundation of China (No. 42305096), the Special
575 Support Plan for High-Level Talents of Guangdong Province (No. 2023JC07L057), the Natural Science Foundation of Guangdong Province (No. 2024A1515011494), the National Key Research and Development Program of China (No. 2023YFC3706204), and the Guangdong Provincial Basic and Applied Basic Research Fund (the Youth Doctoral “Launch” Project) for the Year 2025 (No. SL2024A04J00396). Jianhui Jiang was supported by the National Natural Science Foundation of China (No. 42207122).

580 References

Baier, B. C., Brune, W. H., Lefer, B. L., Miller, D. O., and Martins, D. K.: Direct ozone production rate measurements and their use in assessing ozone source and receptor regions for Houston in 2013, *Atmospheric Environment*, 114, 83-91, doi: 10.1016/j.atmosenv.2015.05.033, 2015.

Baier, B. C., Brune, W. H., Miller, D. O., Blake, D., Long, R., Wisthaler, A., Cantrell, C., Fried, A., Heikes, B., and Brown, S.: Higher measured than modeled ozone production at increased NO_x levels in the Colorado Front Range, *Atmospheric Chemistry and Physics*, 17, 11273-11292, doi: 10.5194/acp-17-11273-2017, 2017.



Cai, C., Geng, F., Tie, X., Yu, Q., and An, J.: Characteristics and source apportionment of VOCs measured in Shanghai, China, *Atmospheric Environment*, 44, 5005-5014, doi: 10.1016/j.atmosenv.2010.07.059, 2010.

590 Cao, Y., Li, Z., Pu, X., Jiang, C., Xue, W., Jiang, H., Zhang, W., and Zhai, C.: Sensitivity of O₃ formation from anthropogenic precursor emissions in typical cities in the Chengdu-Chongqing region: A simulation study, *Acta Scientiae Circumstantiae*, 41, 3001-3011, doi: 10.13671/j.hjkxxb.2021.0207, 2021.

Cazorla, M. and Brune, W.: Measurement of ozone production sensor, *Atmospheric Measurement Techniques Discussions*, 2, 3339-3368, doi: 10.5194/amtd-2-3339-2009, 2009.

595 Cazorla, M., Brune, W., Ren, X., and Lefer, B.: Direct measurement of ozone production rates in Houston in 2009 and comparison with two estimation methods, *Atmospheric Chemistry and Physics*, 12, 1203-1212, doi: 10.5194/acp-12-1203-2012, 2012.

Chen, L., Liao, H., Zhu, J., Li, K., Bai, Y., Yue, X., Yang, Y., Hu, J., and Zhang, M.: Increases in ozone-related mortality in China over 2013–2030 attributed to historical ozone deterioration and future population aging, *Science of The Total Environment*, 858, 159972, doi: 10.1016/j.scitotenv.2022.159972, 2023.

600 Chen, S., Wei, W., Wang, C., Wang, X., Zhou, C., and Cheng, S.: A modeling approach to dynamically estimating local photochemistry process and its contribution to surface O₃ pollution, *Journal of Environmental Management*, 373, 123450, doi: 10.1016/j.jenvman.2024.123450, 2025.

Chen, T., Xue, L., Zheng, P., Zhang, Y., Liu, Y., Sun, J., Han, G., Li, H., Zhang, X., and Li, Y.: Volatile organic compounds and ozone air pollution in an oil production region in northern China, *Atmospheric Chemistry and Physics*, 20, 7069-7086, doi: 605 10.5194/acp-20-7069-2020, 2020a.

Chen, Y., Chi, S., Wang, Y., Guo, S., Zhang, C., Ye, C., and Lin, W.: Ozone production sensitivity in the highland city of Lhasa: a comparative analysis with Beijing, *Air Quality, Atmosphere & Health*, 1-11, doi: 10.1007/s11869-024-01604-4, 2024.

610 Chen, Y., Yan, H., Yao, Y., Zeng, C., Gao, P., Zhuang, L., Fan, L., and Ye, D.: Relationships of ozone formation sensitivity with precursors emissions, meteorology and land use types, in Guangdong-Hong Kong-Macao Greater Bay Area, China, *Journal of Environmental Sciences*, 94, 1-13, doi: 10.1016/j.jes.2020.04.005, 2020b.

Dyson, J. E., Whalley, L. K., Slater, E. J., Woodward-Massey, R., Ye, C., Lee, J. D., Squires, F., Hopkins, J. R., Dunmore, R. E., and Shaw, M.: Impact of HO₂ aerosol uptake on radical levels and O₃ production during summertime in Beijing, *Atmospheric Chemistry and Physics Discussions*, 2022, 1-43, doi: 10.5194/acp-2022-800, 2022.

615 Gilman, J. B., Kuster, W. C., Goldan, P. D., Herndon, S. C., Zahniser, M. S., Tucker, S. C., Brewer, W. A., Lerner, B. M., Williams, E. J., and Harley, R. A.: Measurements of volatile organic compounds during the 2006 TexAQS/GoMACCS campaign: Industrial influences, regional characteristics, and diurnal dependencies of the OH reactivity, *Journal of Geophysical Research: Atmospheres*, 114, doi: 10.1029/2008jd011525, 2009.

Yu, G., Lin L., Xia S., Zhu B., and Huang X.: The characteristics of VOCs and ozone formation sensitivity in a typical industrial area in Shenzhen, *China Environmental Science*, 42, 1994-2001, doi: 10.19674/j.cnki.issn1000-6923.20220112.015, 2022.

620 Hao, Y., Zhou, J., Zhou, J.-P., Wang, Y., Yang, S., Huangfu, Y., Li, X.-B., Zhang, C., Liu, A., and Wu, Y.: Measuring and



modeling investigation of the net photochemical ozone production rate via an improved dual-channel reaction chamber technique, *Atmospheric Chemistry and Physics*, 23, 9891-9910, doi: 10.5194/acp-23-9891-2023, 2023.

Jeffries, H.: An experimental method for measuring the rate of synthesis, destruction, and transport of ozone in the lower atmosphere, Ph. D. Thesis, Department of Environmental Science and Engineering, 1971.

625 Jing, S., Duohong, C., Wang, C., Ridong, C., Yu-jun, L., Yongxi, H., Xin, Z., and Yan, Z.: Study on the Characteristics and Causes of Ozone Severe Pollution Days in Jiangmen City, *China Environmental Science*, 1-19, doi: 10.19674/j.cnki.issn1000-6923.20241212.002, 2024.

630 Kanaya, Y., Hofzumahaus, A., Dorn, H.-P., Brauers, T., Fuchs, H., Holland, F., Rohrer, F., Bohn, B., Tillmann, R., and Wegener, R.: Comparisons of observed and modeled OH and HO₂ concentrations during the ambient measurement period of the HO_x Comp field campaign, *Atmospheric Chemistry and Physics*, 12, 2567-2585, doi: 10.5194/acp-12-2567-2012, 2012.

Li, B., Gasser, T., Ciais, P., Piao, S., Tao, S., Balkanski, Y., Hauglustaine, D., Boisier, J.-P., Chen, Z., and Huang, M.: The contribution of China's emissions to global climate forcing, *Nature*, 531, 357-361, doi: 10.1038/nature17165, 2016.

635 Li, K., Jacob, D. J., Liao, H., Shen, L., Zhang, Q., and Bates, K. H.: Anthropogenic drivers of 2013–2017 trends in summer surface ozone in China, *Proceedings of the National Academy of Sciences*, 116, 422-427, doi: 10.1073/pnas.1812168116, 2019.

640 Li, K., Wang, X., Li, L., Wang, J., Liu, Y., Cheng, X., Xu, B., Wang, X., Yan, P., and Li, S.: Large variability of O₃-precursor relationship during severe ozone polluted period in an industry-driven cluster city (Zibo) of North China Plain, *Journal of Cleaner Production*, 316, 128252, doi: 10.1016/j.jclepro.2021.128252, 2021.

645 Lu, K., Zhang, Y., Su, H., Brauers, T., Chou, C. C., Hofzumahaus, A., Liu, S. C., Kita, K., Kondo, Y., and Shao, M.: Oxidant (O₃+ NO₂) production processes and formation regimes in Beijing, *Journal of Geophysical Research: Atmospheres*, 115, doi: 10.1029/2009JD012714, 2010.

650 Lyu, Y., Gao, Y., Pang, X., Sun, S., Luo, P., Cai, D., Qin, K., Wu, Z., and Wang, B.: Elucidating contributions of volatile organic compounds to ozone formation using random forest during COVID-19 pandemic: A case study in China, *Environmental Pollution*, 346, 123532, doi: 10.1016/j.envpol.2024.123532, 2024.

655 Ma, W., Chen, X., Xia, M., Liu, Y., Wang, Y., Zhang, Y., Zheng, F., Zhan, J., Hua, C., and Wang, Z.: Reactive Chlorine Species Advancing the Atmospheric Oxidation Capacities of Inland Urban Environments, *Environmental Science & Technology*, 57, 14638-14647, doi: 10.1021/acs.est.3c05169, 2023.

660 Ma, W., Feng, Z., Zhan, J., Liu, Y., Liu, P., Liu, C., Ma, Q., Yang, K., Wang, Y., and He, H.: Influence of photochemical loss of volatile organic compounds on understanding ozone formation mechanism, *Atmospheric Chemistry and Physics*, 22, 4841-4851, doi: 10.5194/acp-22-4841-2022, 2022.

665 Mazaheri, M., Lin, W., Clifford, S., Yue, D., Zhai, Y., Xu, M., Rizza, V., and Morawska, L.: Characteristics of school children's personal exposure to ultrafine particles in Heshan, Pearl River Delta, China—A pilot study, *Environment International*, 132, 105134, doi: 10.1016/j.envint.2019.105134, 2019.

Morino, Y., Sadanaga, Y., Sato, K., Sakamoto, Y., Muraoka, T., Miyatake, K., Li, J., and Kajii, Y.: Direct evaluation of the



655 ozone production regime in smog chamber experiments, *Atmospheric Environment*, 309, 119889, doi: 10.1016/j.atmosenv.2023.119889, 2023.

660 Mousavinezhad, S., Choi, Y., Pouyaei, A., Ghahremanloo, M., and Nelson, D. L.: A comprehensive investigation of surface ozone pollution in China, 2015–2019: Separating the contributions from meteorology and precursor emissions, *Atmospheric Research*, 257, 105599, doi: 10.1016/j.atmosres.2021.105599, 2021.

665 Pei, C. L., Xie, Y. T., Chen, X., Zhang, T., Qiu, X. N., Wang, Y., Wang, Z. H., and Li, M.: Analysis of a Typical Ozone Pollution Process in Guangzhou in Winter, *Environmental Science*, 43, 4305-4315, doi: 10.13227/j.hjkx.202110168, 2022.

670 Ren, X., Van Duin, D., Cazorla, M., Chen, S., Mao, J., Zhang, L., Brune, W. H., Flynn, J. H., Grossberg, N., and Lefer, B. L.: Atmospheric oxidation chemistry and ozone production: Results from SHARP 2009 in Houston, Texas, *Journal of Geophysical Research: Atmospheres*, 118, 5770-5780, doi: 10.1002/jgrd.50342, 2013.

675 Sadanaga, Y., Kawasaki, S., Tanaka, Y., Kajii, Y., and Bandow, H.: New system for measuring the photochemical ozone production rate in the atmosphere, *Environmental science & technology*, 51, 2871-2878, doi: 10.1021/acs.est.6b04639, 2017.

680 Sakamoto, Y., Sadanaga, Y., Li, J., Matsuoka, K., Takemura, M., Fujii, T., Nakagawa, M., Kohno, N., Nakashima, Y., and Sato, K.: Relative and absolute sensitivity analysis on ozone production in Tsukuba, a city in Japan, *Environmental science & technology*, 53, 13629-13635, doi: 10.1021/acs.est.9b03542, 2019.

Sklaveniti, S., Locoge, N., Stevens, P. S., Wood, E., Kundu, S., and Dusanter, S.: Development of an instrument for direct ozone production rate measurements: Measurement reliability and current limitations, *Atmospheric Measurement Techniques*, 11, 741-761, doi: 10.1029/98jd00349, 2018.

685 Sommariva, R., Cox, S., Martin, C., Borońska, K., Young, J., Jimack, P. K., Pilling, M. J., Matthaios, V. N., Nelson, B. S., and Newland, M. J.: AtChem (version 1), an open-source box model for the Master Chemical Mechanism, *Geoscientific Model Development*, 13, 169-183, doi: 10.5194/gmd-13-169-2020, 2020.

Song, K., Liu, R., Wang, Y., Liu, T., Wei, L., Wu, Y., Zheng, J., Wang, B., and Liu, S. C.: Observation-based analysis of ozone production sensitivity for two persistent ozone episodes in Guangdong, China, *Atmospheric Chemistry and Physics*, 22, 8403-8416, doi: 10.5194/acp-22-8403-2022, 2022.

690 Tan, Z., Fuchs, H., Lu, K., Hofzumahaus, A., Bohn, B., Broch, S., Dong, H., Gomm, S., Häseler, R., and He, L.: Radical chemistry at a rural site (Wangdu) in the North China Plain: observation and model calculations of OH, HO₂ and RO₂ radicals, *Atmospheric Chemistry and Physics*, 17, 663-690, doi: 10.5194/acp-17-663-2017, 2017.

Tan, Z., Lu, K., Dong, H., Hu, M., Li, X., Liu, Y., Lu, S., Shao, M., Su, R., and Wang, H.: Explicit diagnosis of the local ozone production rate and the ozone-NO_x-VOC sensitivities, *Science bulletin*, 63, 1067-1076, doi: 10.1016/j.scib.2018.07.001, 2018.

695 Tan, Z., Lu, K., Hofzumahaus, A., Fuchs, H., Bohn, B., Holland, F., Liu, Y., Rohrer, F., Shao, M., and Sun, K.: Experimental budgets of OH, HO₂, and RO₂ radicals and implications for ozone formation in the Pearl River Delta in China 2014, *Atmospheric chemistry and physics*, 19, 7129-7150, doi: 10.5194/acp-2018-801, 2019.

Tong, J., Hu, R., Hu, C., Liu, X., Cai, H., Lin, C., Zhong, L., Wang, J., and Xie, P.: Development of a net ozone production



rate detection system based on dual-channel cavity ring-down spectroscopy, *Journal of Environmental Sciences*, 149, 419-430,
690 doi: 10.1016/j.jes.2024.01.035, 2025.

Wang, J., Zhang, Y., Wu, Z., Luo, S., Song, W., and Wang, X.: Ozone episodes during and after the 2018 Chinese National
Day holidays in Guangzhou: Implications for the control of precursor VOCs, *Journal of Environmental Sciences*, 114, 322-
333, doi: 10.1016/j.jes.2021.09.009, 2022a.

Wang, R., Wang, L., Sun, J., Zhang, L., Li, Y., Li, K., Liu, B., Zhang, J., and Wang, Y.: Maximizing ozone control by spatial
695 sensitivity-oriented mitigation strategy in the Pearl River Delta Region, China, *Science of The Total Environment*, 905, 166987,
doi: 10.1016/j.scitotenv.2023.166987, 2023.

Wang, T., Xue, L., Brimblecombe, P., Lam, Y. F., Li, L., and Zhang, L.: Ozone pollution in China: A review of concentrations,
meteorological influences, chemical precursors, and effects, *Science of the Total Environment*, 575, 1582-1596, doi:
10.1016/j.scitotenv.2016.10.081, 2017.

700 Wang, W., Li, X., Cheng, Y., Parrish, D. D., Ni, R., Tan, Z., Liu, Y., Lu, S., Wu, Y., and Chen, S.: Ozone pollution mitigation
strategy informed by long-term trends of atmospheric oxidation capacity, *Nature Geoscience*, 17, 20-25, doi: 10.1038/s41561-
023-01334-9, 2024a.

Wang, W., Yuan, B., Peng, Y., Su, H., Cheng, Y., Yang, S., Wu, C., Qi, J., Bao, F., and Huangfu, Y.: Direct observations indicate
705 photodegradable oxygenated volatile organic compounds (OVOCs) as larger contributors to radicals and ozone production in
the atmosphere, *Atmospheric Chemistry and Physics*, 22, 4117-4128, doi: 10.5194/acp-22-4117-2022, 2022b.

Wang, W., Yuan, B., Su, H., Cheng, Y., Qi, J., Wang, S., Song, W., Wang, X., Xue, C., and Ma, C.: A large role of missing
volatile organic compound reactivity from anthropogenic emissions in ozone pollution regulation, *Atmospheric Chemistry and
710 Physics*, 24, 4017-4027, doi: 10.5194/acp-24-4017-2024, 2024b.

Wang, Y., Chen, Y., Chi, S., Wang, J., Zhang, C., Lin, W., Zhao, W., and Ye, C.: Optimizing a twin-chamber system for direct
ozone production rate measurement, *Environmental Pollution*, 348, 123837, doi: 10.1016/j.envpol.2024.123837, 2024c.

Wei, N., Zhao, W., Yao, Y., Wang, H., Liu, Z., Xu, X., Rahman, M., Zhang, C., Fittschen, C., and Zhang, W.: Peroxy radical
chemistry during ozone photochemical pollution season at a suburban site in the boundary of Jiangsu–Anhui–Shandong–
715 Henan region, China, *Science of the Total Environment*, 904, 166355, doi: 10.1016/j.scitotenv.2023.166355, 2023.

Whalley, L. K., Slater, E. J., Woodward-Massey, R., Ye, C., Lee, J. D., Squires, F., Hopkins, J. R., Dunmore, R. E., Shaw, M.,
720 and Hamilton, J. F.: Evaluating the sensitivity of radical chemistry and ozone formation to ambient VOCs and NO_x in Beijing,
Atmospheric Chemistry and Physics, 21, 2125-2147, doi: 10.5194/acp-2020-785, 2021.

Woodward-Massey, R., Sommariva, R., Whalley, L. K., Cryer, D. R., Ingham, T., Bloss, W. J., Ball, S. M., Cox, S., Lee, J. D.,
and Reed, C. P.: Radical chemistry and ozone production at a UK coastal receptor site, *Atmospheric Chemistry and Physics*,
23, 14393-14424, doi: 10.5194/acp-23-14393-2023, 2023.

725 Wu, C., Wang, C., Wang, S., Wang, W., Yuan, B., Qi, J., Wang, B., Wang, H., Wang, C., Song, W., Wang, X., Hu, W., Lou, S.,
Ye, C., Peng, Y., Wang, Z., Huangfu, Y., Xie, Y., Zhu, M., Zheng, J., Wang, X., Jiang, B., Zhang, Z., and Shao, M.: Measurement
report: Important contributions of oxygenated compounds to emissions and chemistry of volatile organic compounds in urban



air, *Atmospheric Chemistry and Physics*, 20, 14769-14785, doi: 10.5194/acp-20-14769-2020, 2020.

Xu, D., Yuan, Z., Wang, M., Zhao, K., Liu, X., Duan, Y., Fu, Q., Wang, Q., Jing, S., and Wang, H.: Multi-factor reconciliation of discrepancies in ozone-precursor sensitivity retrieved from observation-and emission-based models, *Environment International*, 158, 106952, doi: 10.1016/j.envint.2021.106952, 2022.

Yadav, P., Lal, S., Tripathi, S. N., Jain, V., and Mandal, T. K.: Role of sources of NMVOCs in O₃, OH reactivity, and secondary organic aerosol formation over Delhi, *Atmospheric Pollution Research*, 15, 102082, doi: 10.1016/j.apr.2024.102082, 2024.

Yang, M., Li, F., Huang, C., Tong, L., Dai, X., and Xiao, H.: VOC characteristics and their source apportionment in a coastal industrial area in the Yangtze River Delta, China, *Journal of Environmental Sciences*, 127, 483-494, doi: 10.1016/j.jes.2022.05.041, 2023.

Yang, X., Lu, K., Ma, X., Gao, Y., Tan, Z., Wang, H., Chen, X., Li, X., Huang, X., and He, L.: Radical chemistry in the Pearl River Delta: observations and modeling of OH and HO₂ radicals in Shenzhen 2018, *Atmospheric Chemistry and Physics Discussions*, 2022, 1-19, doi: 10.5194/acp-22-12525-2022, 2022.

Yang, Y., Shao, M., Keßel, S., Li, Y., Lu, K., Lu, S., Williams, J., Zhang, Y., Zeng, L., and Nölscher, A. C.: How the OH reactivity affects the ozone production efficiency: case studies in Beijing and Heshan, China, *Atmospheric Chemistry and Physics*, 17, 7127-7142, doi: 10.5194/acp-17-7127-2017, 2017.

Yu, D., Tan, Z., Lu, K., Ma, X., Li, X., Chen, S., Zhu, B., Lin, L., Li, Y., and Qiu, P.: An explicit study of local ozone budget and NO_x-VOCs sensitivity in Shenzhen China, *Atmospheric Environment*, 224, 117304, doi: 10.1016/j.atmosenv.2020.117304, 2020.

Zhang, G., Yu, X., Yin, H., Feng, C., Ma, C., Sun, S., Cheng, H., Wang, S., Shang, K., and Liu, X.: Heatwave-amplified atmospheric oxidation in a multi-province border area in Xuzhou, China, *Frontiers in Environmental Science*, 12, 1496584, doi: 10.3389/fenvs.2024.1496584, 2024.

Zhang, L., Brook, J. R., and Vet, R.: A revised parameterization for gaseous dry deposition in air-quality models, *Atmospheric Chemistry and Physics*, 3, 2067-2082, doi: 10.5194/acp-3-2067-2003, 2003.

Zhang, Y., Xue, L., Chen, T., Shen, H., Li, H., and Wang, W.: Development history of Observation-Based Model (OBM) and its application and prospect in atmospheric chemistry studies in China, *Res. Environ. Sci.*, 35, 621-632, doi: 10.13198/j.issn.1001-6929.2022.01.05, 2022.

Zheng, S., Xu, X., Zhang, Y., Wang, L., Yang, Y., Jin, S., and Yang, X.: Characteristics and sources of VOCs in urban and suburban environments in Shanghai, China, during the 2016 G20 summit, *Atmospheric Pollution Research*, 10, 1766-1779, doi: 10.1016/j.apr.2019.07.008, 2019.

Zhou, J., Sato, K., Bai, Y., Fukusaki, Y., Kousa, Y., Ramasamy, S., Takami, A., Yoshino, A., Nakayama, T., and Sadanaga, Y.: Kinetics and impacting factors of HO₂ uptake onto submicron atmospheric aerosols during the 2019 Air QUAlity Study (AQUAS) in Yokohama, Japan, *Atmospheric Chemistry and Physics*, 21, 12243-12260, doi: 10.5194/acp-21-12243-2021, 2021.

Zhou, J., Wang, W., Wang, Y., Zhou, Z., Lv, X., Zhong, M., Zhong, B., Deng, M., Jiang, B., and Luo, J.: Intercomparison of



measured and modelled photochemical ozone production rates: Suggestion of chemistry hypothesis regarding unmeasured VOCs, *Science of The Total Environment*, 951, 175290, doi: 10.1016/j.scitotenv.2024.175290, 2024a.

Zhou, J., Zhang, C., Liu, A., Yuan, B., Wang, Y., Wang, W., Zhou, J.-P., Hao, Y., Li, X.-B., and He, X.: Measurement report: 760 Vertical and temporal variability in the near-surface ozone production rate and sensitivity in an urban area in the Pearl River Delta region, China, *Atmospheric Chemistry and Physics*, 24, 9805-9826, doi: 10.5194/acp-24-9805-2024, 2024b.